Original Article

# Numerical convergence and validation of the DIMP inverse particle transport model☆

Noel Nelson*, Yousry Azmy

*North Carolina State University, Box 7909, Raleigh, NC 27695, USA*

ABSTRACT

The data integration with modeled predictions (DIMP) model is a promising inverse radiation transport method for solving the special nuclear material (SNM) holdup problem. Unlike previous methods, DIMP is a completely passive nondestructive assay technique that requires no initial assumptions regarding the source distribution or active measurement time. DIMP predicts the most probable source location and distribution through Bayesian inference and quasi-Newtonian optimization of predicted detector responses (using the adjoint transport solution) with measured responses. DIMP performs well with forward hemispherical collimation and unshielded measurements, but several considerations are required when using narrow-view collimated detectors. DIMP converged well to the correct source distribution as the number of synthetic responses increased. DIMP also performed well for the first experimental validation exercise after applying a collimation factor, and sufficiently reducing the source search volume's extent to prevent the optimizer from getting stuck in local minima. DIMP's simple point detector response function (DRF) is being improved to address coplanar false positive/negative responses, and an angular DRF is being considered for integration with the next version of DIMP to account for highly collimated responses. Overall, DIMP shows promise for solving the SNM holdup inverse problem, especially once an improved optimization algorithm is implemented.
© 2017 Korean Nuclear Society, Published by Elsevier Korea LLC. This is an open access article under the CC BY-NC-ND license (http://creativecommons.org/licenses/by-nc-nd/4.0/).

## 1. Introduction

The goal of this work is to validate the data integration with modeled predictions (DIMP) inverse particle transport method for solving the special nuclear material (SNM) holdup problem. Holdup problems arise when radioactive material (with a known emission spectrum) becomes trapped in processing equipment at nuclear fuel processing facilities. Examples of processing equipment can include, but are not limited to, pipes, ducts and filters, glove boxes, and valves [2]. SNM holdup is of interest to the nuclear fuel industry for many reasons, including criticality safety, maintaining accurate SNM inventory and complying with nuclear safeguards regimes, and ensuring radiation worker safety.

Therefore, it is important to quantify holdup sources in total material mass as well as distribution and location. The DIMP method offers a well-automated system that poses the holdup configuration as an inverse problem. Initial survey crews are not required, and few assumptions are necessary to predict source distribution, strength, and location within equipment. DIMP uses an adjoint particle transport model to calculate an importance map for a grid of detectors in the target geometric configuration, utilizing as-built information regarding dimensions and material composition of the facility's structure. Deterministic transport codes are capable of modeling such configurations, with varying degrees of fidelity of the models to achieve the desired computational accuracy. Together, the computed flux and detector response functions can be used to predict detector responses from a given source distribution. Alternatively, and more efficiently in the present case, folding the importance function with a given source distribution yields an estimate of the detector response where the importance function is the adjoint flux computed with an adjoint source set to that detector's response function. DIMP calculates the optimal source distribution(s), location(s), and strength(s) that best match calculated responses to experimental responses with no presumptions about the source shape, and applying minimal obvious restrictions on its physical location, e.g., a source cannot be hanging in the air in the middle of a room.

Currently, the DIMP model has been validated for a Cs-137 point source and a Co-60 line source. It performed well in predicting the

---

sources' spatial distributions with low error that was mostly attributed to the weakness of the available sources (older button sources) [3]. This work intends to expand upon the model and previous research with realistic holdup experiments using strong uranium sources measured with a field holdup NaI detector, and eventually to compare the results to the Holdup Measurement System (HMS-4), a generalized geometry holdup (GGH) model. Four experimental holdup measurement campaigns are performed in this work including a Cs-137 point source, a highly enriched uranium (HEU) disk source, an HEU line source in a pipe, and a set of HEU area sources in a duct.

## 2. Theory: DIMP formalism

Inverse problems are often very complex and ill-conditioned. For such problems, information at various points in space and time denoted "measurements" are considered known, but the source state or its spatial configuration is treated as unknown. An inverse model is used to calculate a possible solution state of the system from the measurements. This is where the difficulty of inverse problems arises. The existence and uniqueness of an inverse solution is typically not certain, and solutions can be very unstable depending on the complexity of the model and the optimization method implemented.

One way to address the difficulty of inverse problems is to find solutions with probabilistic methods. While the solution that best fits the measurement data is not always the true solution, the chance that it is the true solution should increase with an increasing amount of measured data. This idea is formalized via Bayes' theorem [4]:

$$p(hypothesis|data, I) \propto p(data|hypothesis, I)p(hypothesis|I), \quad (1)$$

where *data* is the experimentally measured data (e.g., detector responses), the *hypothesis* is the unknowns of the system (source parameters in this work), and *I* is all the additional knowledge of the system (system geometry, detector efficiency, detector response functions, etc.). The three probability density functions (PDFs) above $p(hypothesis|data,I)$, $p(data|hypothesis,I)$, and $p(hypothesis|I)$ are the posterior, likelihood, and prior, respectively. The prior is the conditional probability that the hypothesis occurs based only on information *I*. The likelihood represents the probability of measurement data occurring based on a given configuration of the unknown data (hypothesis) and the information in *I*. This is proportional to the posterior, or the probability of the given *hypothesis* (source configuration) being true based on the information *I* and the measurement *data*.

In order to solve an inverse problem, the likelihood function is maximized, thereby minimizing the error between the experimentally measured data and the synthetic responses (results computed by a completely different radiation transport solution method using a model of the geometric configuration of the experiment and the true source parameters). DIMP maximizes agreement between the measurement vector $\boldsymbol{r}_m$ (responses) and the modeled responses, $\boldsymbol{r}_p$, predicted by a configuration of the model parameters, $\alpha$

$$\boldsymbol{r}_m = R\alpha \quad (2)$$

where *R* is the mapping operator from the model parameter input space to the response space. The solution of this problem is linear for radiation transport and has a closed form solution for the posterior means and covariances. Cacuci's best estimate method based on Bayesian inference is used to find the posterior solution mean and uncertainty [5].

## 2.1. Radiation transport

First, the model used in the inverse problem framework will be described in detail, followed by specification of the source parameters contained in $\alpha$ and a few notes on the measurements $\boldsymbol{r}_m$. The model for the radiation transport problem is based on the time independent linear Boltzmann transport equation for neutral particles in non-multiplying media [6]

$$\widehat{\Omega} \cdot \nabla \psi\left(\boldsymbol{x}, E, \widehat{\Omega}\right) + \sigma(\boldsymbol{x}, E)\psi\left(\boldsymbol{x}, E, \widehat{\Omega}\right)$$
$$= \int dE' \int d\widehat{\Omega}' \sigma_s\left(\boldsymbol{x}; E', \widehat{\Omega}' \to E, \widehat{\Omega}\right)\psi\left(\boldsymbol{x}, E', \widehat{\Omega}'\right) + q\left(\boldsymbol{x}, E, \widehat{\Omega}\right), \quad (3)$$

where $\psi(\boldsymbol{x}, E, \widehat{\Omega})$ is the angular flux of particles [*particles*/$cm^2$-*s*] defined over the spatial domain $x \in V$, $\widehat{\Omega} \in 4\pi$, $E \in (0, \infty)$, and with explicit boundary conditions $\psi(\boldsymbol{x}, E, \widehat{\Omega}) = \psi_0(\boldsymbol{x}, E, \widehat{\Omega})$ for $\boldsymbol{x} \in \partial V$ and $\widehat{\Omega} \cdot \widehat{n} < 0$. $\widehat{\Omega}$ is the unit directional vector along which particles are traveling, $\widehat{n}$ is the unit vector normal to the boundary surface $\partial V$ at the point $\boldsymbol{x}$, and $\sigma(\boldsymbol{x}, E)$ is the total particle interaction macroscopic cross-section [$cm^{-1}$]. Additionally, $\sigma_s(\boldsymbol{x}; E', \widehat{\Omega}' \to E, \widehat{\Omega})$ is the macroscopic scattering cross-section of particles from one direction $(\widehat{\Omega}')$ and energy $(E')$ in the direction and energy range of $d\widehat{\Omega}'$, $dE'$ about the direction and energy of interest $(\widehat{\Omega}, E)$, and $q(\boldsymbol{x}, E, \widehat{\Omega})$ is the external source of radiation particles in the configuration of interest [in *particles*/$cm^3$-*s*]. In DIMP the geometric configuration and material composition of all objects in the problem domain are considered known, hence the multigroup cross-sections are retrieved and calculated for nuclide mixtures by MAVRIC [7]. Next, it is useful to define the scalar flux $\phi(\boldsymbol{x},E)$ as

$$\phi(\boldsymbol{x}, E) = \int_{4\pi} d\widehat{\Omega}\psi\left(\boldsymbol{x}, E, \widehat{\Omega}\right). \quad (4)$$

Reaction rates are key components to many radiation problems, such as dose and fission rates. In this case, the reaction rate definition is used to define a detector response, *r*, as

$$r(E') = \int_0^\infty dE \int_V d\boldsymbol{x}\sigma_d(\boldsymbol{x}, E', E)\phi(\boldsymbol{x}, E), \quad (5)$$

where $\sigma_d(\boldsymbol{x},E',E)$ is the detector response function (DRF). There are several ways to model and define DRFs, and this is currently under active consideration. In Eq. [5], $\sigma_d(\boldsymbol{x},E',E)$ is the probability per unit path length that a particle at $\boldsymbol{x}$ incident with energy *E* registers a response in the detector's channel dedicated to energy *E'*. With this definition in mind, it would be possible to use the inverse of the forward transport equation, Eq. [3] as the mapping function for the inverse problem. However, direct inverses are often numerically unstable and computationally expensive. Alternatively, the solution of the inverse problem is obtained by searching for a source distribution that best matches the measured responses. Eq. [5] requires a solution of the transport equation for every potential source distribution in order to determine the corresponding $\phi(\boldsymbol{x},E)$, then compute *r* and compare it to the measured values. Alternatively, the problem can be reformulated using the adjoint of the transport equation [3]. The adjoint identity can be stated as

$$\langle Ap, h \rangle = \langle p, A^\dagger h \rangle, \quad (6)$$

where $\langle, \rangle$ denotes an inner product, *A* is an operator, *p* and *h* are any pair of functions in the domain of *A*, and $A^\dagger$ is the adjoint operator. Furthermore, in this application we define the inner product as follows

$$\langle p, h \rangle = \int\limits_{4\pi} d\widehat{\Omega} \int\limits_0^\infty dE \int\limits_V dV p\left(\boldsymbol{x}, E, \widehat{\Omega}\right) h\left(\boldsymbol{x}, E, \widehat{\Omega}\right). \tag{7}$$

Now, consider the fixed source linear transport equation in operator form

$$L\psi = q, \tag{8}$$

where $L$ is the transport operator (for all angular fluxes, $\psi$), and $q$ is the external source. Next, take the inner product of Eq. [8] with the adjoint angular flux $\psi^\dagger$ (to be defined shortly)

$$\langle L\psi, \psi^\dagger \rangle = \langle q, \psi^\dagger \rangle. \tag{9}$$

Applying the adjoint identity [Eq. [6]] to the above equation yields [6]

$$\langle L\psi, \psi^\dagger \rangle = \langle \psi, L^\dagger \psi^\dagger \rangle + P\left[\psi, \psi^\dagger\right], \tag{10}$$

where $P[\psi, \psi^\dagger]$ is the bilinear concomitant, evaluated on the external surface of volume $V$,

$$P\left[\psi, \psi^\dagger\right] = \int\limits_{4\pi} d\widehat{\Omega} \int\limits_0^\infty dE \int\limits_{\partial V} dS\widehat{\Omega} \cdot \widehat{n}\psi\left(\boldsymbol{x}, E, \widehat{\Omega}\right)\psi^\dagger\left(\boldsymbol{x}, E, \widehat{\Omega}\right). \tag{11}$$

Substituting Eq. [10] into Eq. [9] yields

$$\langle \psi, L^\dagger \psi^\dagger \rangle = \langle q, \psi^\dagger \rangle - P\left[\psi, \psi^\dagger\right]. \tag{12}$$

Next we set the adjoint source to the detector response function, namely $q^\dagger = \sigma_d$, implying

$$L^\dagger \psi^\dagger = \sigma_d. \tag{13}$$

Substituting this relationship into Eq. [12] yields

$$\langle \psi, \sigma_d \rangle = \langle q, \psi^\dagger \rangle - P\left[\psi, \psi^\dagger\right]. \tag{14}$$

Now, applying the following vacuum boundary conditions

$$\psi\left(\boldsymbol{x}, E, \widehat{\Omega}\right) = 0; for \ \boldsymbol{x} \in \partial V \ and \ \widehat{\Omega} \cdot \widehat{n} < 0, \tag{15}$$

$$\psi^\dagger\left(\boldsymbol{x}, E, \widehat{\Omega}\right) = 0; for \ \boldsymbol{x} \in \partial V \ and \ \widehat{\Omega} \cdot \widehat{n} > 0, \tag{16}$$

will cause the bilinear concomitant term to vanish, thus producing

$$\langle \psi, \sigma_d \rangle = \langle q, \psi^\dagger \rangle \tag{17}$$

Finally, recalling the reaction rate Eq. [5] and substituting it in Eq. (17) leads to

$$\boldsymbol{r}_p(E) = \int\limits_0^\infty dE \int\limits_V dV \phi^\dagger(\boldsymbol{x}, E) q(\boldsymbol{x}, E) \tag{18}$$

where $\phi^\dagger(\boldsymbol{x}, E)$ is the adjoint scalar flux, or importance, and $\boldsymbol{r}_p(E)$ is the model-predicted response. The advantage of the formulation in Eq. (18) over the one in Eq. [5] is the computationally inexpensive evaluation of the former once $\phi^\dagger$ is known for a set of detectors. During the search for an optimal source distribution, Eq. (18) comprises an inner product of the precomputed adjoint fluxes and a guess regarding the source distribution. In contrast, Eq. [5]

requires a full forward transport solution for every attempted source distribution. The set of discretized importance values are calculated by the discrete ordinates package DENOVO [7] using $S_n = 8$ and 23 photon groups, and they are folded with the predicted source distribution ($q(\boldsymbol{x}, E)$) during the search for the best match between the resulting responses and the measurement responses $\boldsymbol{r}_m$. The quadrature was chosen as a compromise between accuracy and computational efficiency, and DENOVO's first collision source option was implemented to mitigate ray effects in air. The cross-sections for DENOVO are generated by MAVRIC (part of ORNL's SCALE package) from the Evaluated Nuclear Data Files (200n-47g ENDF/B-VII.0) libraries. The optimal source distribution is found through an optimization process that if successfully converged, yields $\boldsymbol{r}_p(E) \cong \boldsymbol{r}_m(E)$, and in this case we call the corresponding $q(\boldsymbol{x}, E)$ a solution to the inverse problem.

Currently, only the peak responses are compared for both predicted and measured responses. A full response comparison was attempted in previous work [8] including the continuum and peak responses, but the continuum response was very difficult to calculate. Accurate representation of the continuum response requires a fairly sophisticated DRF. Some research has been invested in the area of DRFs for unshielded detectors [9], but more development of the DRF is required to apply it to collimated detector responses as shown by Nelson [10].

### 2.2. Nonlinear optimization

In order to optimize the predicted source distribution, the posterior probability is maximized by minimizing the residual ($Q(\boldsymbol{z})$) of the difference vector ($\boldsymbol{z}$), which contains the absolute differences in the model parameters from the initial guess and those between the measured and predicted responses. The optimization method implemented in this work is the gradient based quasi-Newton method with the best estimate covariance as described by Cacuci and Jonescu-Bujor [5]. The method works by minimizing $Q(\boldsymbol{z})$ according to nonlinear least squares using the following Newton update step for the $k^{th}$ iteration

$$\boldsymbol{\alpha}_{k+1} = \boldsymbol{\alpha}_k - \lambda_k \left(\nabla_\alpha^2 Q(\boldsymbol{z}_k)\right)^{-1} \nabla_\alpha Q(\boldsymbol{z}_k), k = 0, 1, \ldots \tag{19}$$

where $\lambda_k \in [0,1]$ is the line search parameter which controls the search step size. $\boldsymbol{\alpha}_k$ is the source spatial distribution written in vector form (model parameters) for all peak energies at iteration $k$, and $\alpha_0$ is the priori or initial guess. The gradient of $Q$ is

$$\nabla_\alpha Q(\boldsymbol{z}) = C_\alpha^{-1} \boldsymbol{z}_\alpha + S^T C_m^{-1} \boldsymbol{z}_r \tag{20}$$

where $C_\alpha$, $C_m$, and $S$ are the source distribution and measurement covariance matrices, and the collective matrix of adjoint sensitivities ($\phi^\dagger(E)$), respectively, as defined by Hykes [8]. Under the Gauss−Newton approximation, the Hessian is defined as

$$\nabla_\alpha^2 Q(\boldsymbol{z}) \approx C_\alpha^{-1} + S^T C_m^{-1} S \tag{21}$$

where the inverses of the covariance matrices are replaced by the appropriate linear systems of equations (consult Hykes [8]) and solved for efficiency using standard linear methods (e.g., Gaussian partial pivoting). Finally, the functional of the difference vector, $Q(\boldsymbol{z})$ is then defined as

$$Q(\boldsymbol{z}) = \boldsymbol{z}^T C^{-1} \boldsymbol{z}, \tag{22}$$

and the inverse of the covariance, $C^{-1}$, is

$$C^{-1} = \begin{bmatrix} C_\alpha^{-1} & 0 \\ 0 & C_m^{-1} \end{bmatrix}. \tag{23}$$

The difference vector, $z$ is

$$z \equiv \begin{bmatrix} \alpha - \alpha^0 \\ r_p - r_m \end{bmatrix} = \begin{bmatrix} z_\alpha \\ z_r \end{bmatrix} \tag{24}$$

where $r_p$ is the response calculated with the attempted source distribution and $r_m$ is the measured response.

## 3. Results and analysis

Several simulations of radiation sources in various geometries have been performed with DIMP. To confirm the stability of the DIMP method, several simulations of a source configuration were performed using synthetic responses while increasing the number of detection points per simulation in order to verify if DIMP converges to the true solution, i.e., the source used to compute the synthetic responses.

### 3.1. Preliminary convergence studies

A preliminary convergence study was performed involving only the Cs-137 point source using three to nine detection points. DIMP converged and performed well for this case, resolving the source to the cell with the true coordinate location and a neighboring cell and determining the source strength within 0.7% of its true value. These small errors in the DIMP solution are to be expected due to the different computational models applied to the computation of detector responses (Monte Carlo) and the adjoint responses (discrete ordinates), and are representative of measurement errors. Another numerical study was performed with synthetic responses for the Cs-137 and Co-60 sources using only unshielded detector responses, and another using only directional responses. DIMP performed adequately with directional responses, but failed to resolve the unknown source using only unshielded responses due to the optimizer becoming trapped in local minima. If an initial guess close to the true source configuration was supplied, the global minimum was found by DIMP producing the correct answer with a greatly reduced chi-squared value. This suggests that the DIMP gradient-based optimizer only yielded a local minimum when the original initial guess was supplied. Adaptive meshing and
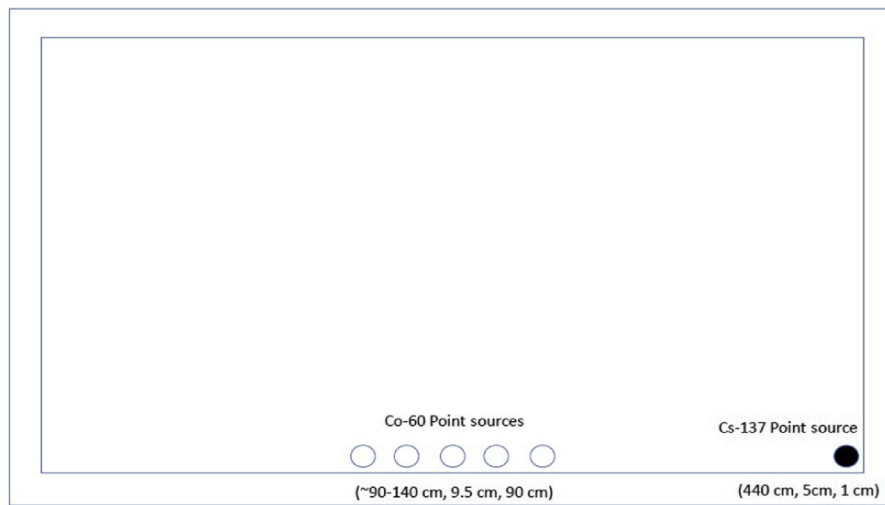


Fig. 1. Rough 2D section of the layout of the simulation geometry of Burlington 2144 at NC State University.
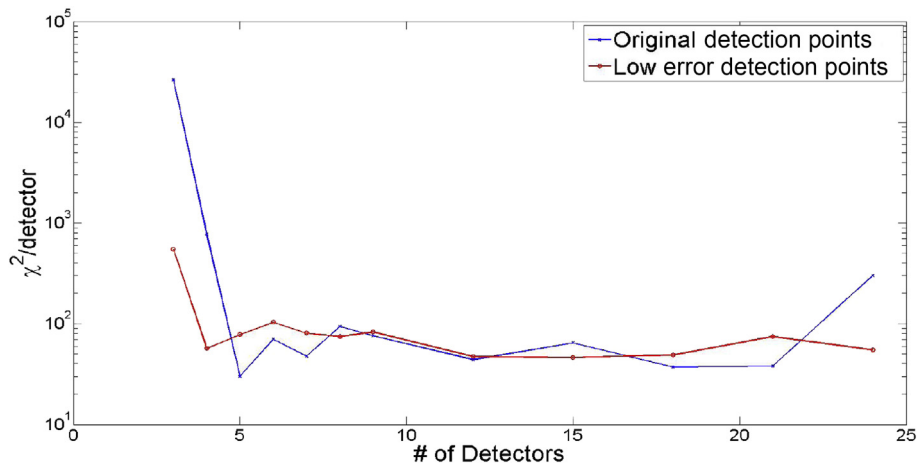


Fig. 2. Comparison of the reduced chi-squared per detector as a function of an increasing number of detection points for the original 24 detectors and a low-error detector responses set.

alternative optimization methods are being explored for DIMP to avoid this issue.

### 3.2. DIMP convergence with multiple sources

The convergence test involved the original source setup used by Hykes and Azmy [3] depicting a Cs-137 point source and five Co-60 point sources located at two separate locations in a room at NC State University. The basic source layout is shown in Fig. 1.

Initial results indicated that DIMP seemed to diverge beyond 21 detection points for this case. This anomaly was further investigated, and the reason for the divergence was isolated to poor agreement between one detector response predicted by DENOVO compared to the corresponding MCNP synthetic response. This response was overlooked because it was a detection point, coplanar (in xy) with one of the Co-60 point sources originally chosen in the Hykes and Azmy experiment [3]. The DIMP DRF produced a false positive and negative result in the z-directional predicted responses from DENOVO for that point. Upon replacement of the detection point with a low error detection point that is off-plane for all cells, DIMP converged with fairly stable results.

For the purposes of this convergence study only synthetic measurements generated with MCNP were used as detector responses, where the number of detection points was increased from 3 to 24 points in total. Each detection point consists of seven measurements: an unshielded detector response and six collimated directional detector responses along the coordinate axes (e.g., +x, −x, etc.) [3]. The results of the convergence study are shown in Figs. 2−6. The true location and strength of the Cs-137 point source is [440,5,1] cm, and the corresponding strength is 107.685 kBq. The true location of the Co-60 line source is centered at approximately (120, 9.525, 90.17) cm. The individual x-co-ordinates of the five point sources that compose the line source are x = 96.52, 107.95, 119.38, 130.175, and 143.764 cm, and their strengths are 0.525, 2.218, 5.767, 31.793, and 3.845 kBq, respectively. Note, DIMP treats the two coincident photons from Co-60 as independent sources with no correlation in space. Therefore, each Co source cell mapped by DIMP from one energy can be in the same cell or a different cell from the ones of the other energy.

The reduced chi-squared is normalized per detector in order to screen out the expected modeling error between DENOVO adjoint based responses and MCNP responses that accumulate with the addition of each detector. As evidenced by the large error in the predicted source locations, weak strengths, and the resulting very large chi-squared-per-detector values, DIMP did not perform adequately with fewer than five detectors for this source
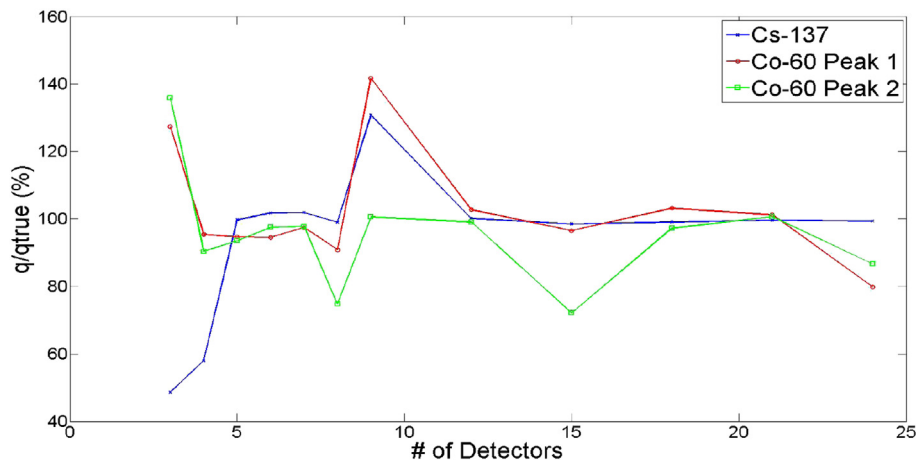


**Fig. 3.** Total predicted source strength across all cells above 1% relative to the total true source strength as a function of increasing detection points using the original 24 detection points.
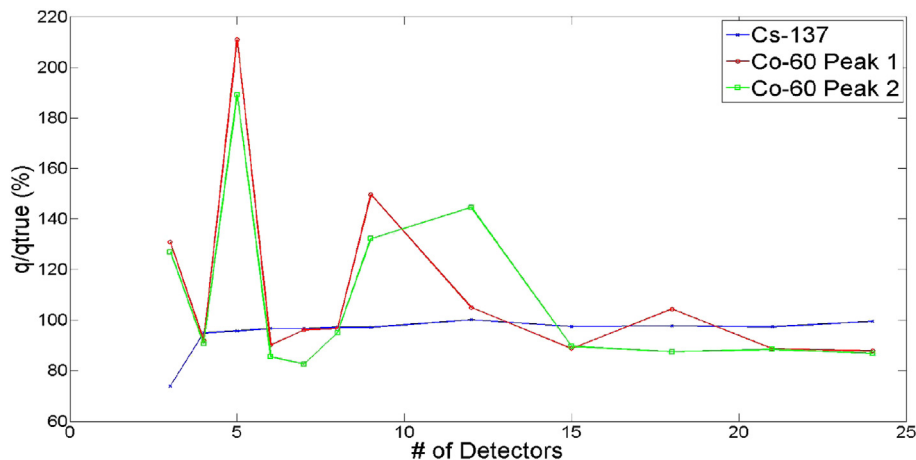


**Fig. 4.** Total predicted source strength across all cells above 1% relative to the total true source strength as a function of increasing detection points using the low-error detection points.
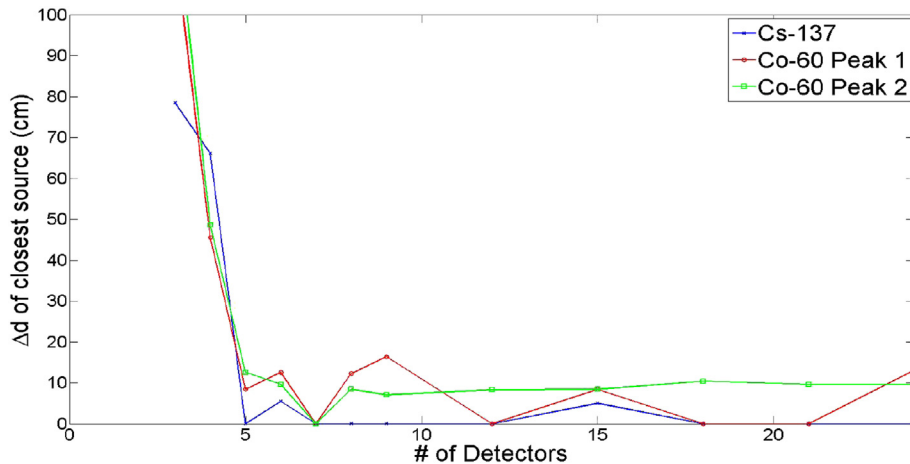
**Fig. 5.** Distance between the predicted source cell and the true source cell (Δ*d*) as a function of increasing detection points using the original 24 detection points. Note: the location of the closest cell of the predicted set is compared to the strongest Co-60 point source location.
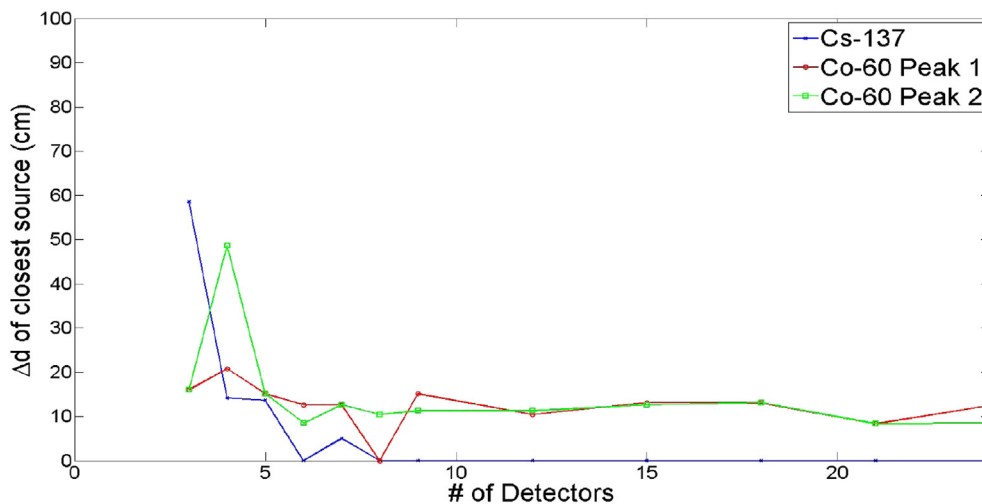


**Fig. 6.** Distance between the predicted source cell and the true source cell (Δ*d*) as a function of increasing detection points using the low-error detection points. Note: the location of the closest cell of the predicted set is compared to the strongest Co-60 point source location.

configuration. With so few detectors, the code placed the source near to one of the detectors. DIMP did not converge with fewer than five detectors for this source configuration comprising a six-point distribution with three distinct energies. Beyond seven detectors, the low-error detection points curve decreased gradually and flattened off suggesting convergence, instead of the unstable divergence of the previous set. Each source configuration consisted of activities (in Bq) calculated across a $52 \times 53 \times 54$ mesh employed in the DENOVO model of the room's configuration, where the predicted source strength exceeded 1% of the source's known true strength, along with its strength relative to that of the true strength used in generating the synthetic responses (Figs. 3 and 4) and the distance from its true location (Δ*d*) to the mesh cell center (as shown in Figs. 5 and 6).

Similar gradually decreasing and fairly flat curves can be observed for the low-error sets of the relative source strength and distance graphs. From 5–7 detectors, the Cs-137 point source is well resolved, merely wavering between two configurations: a 50/50 split of the source with the correct cell and a neighboring cell and most of the source strength (>70%) concentrated in one of these two cells. The Co-60 line source however, is only resolved as one- or two-cell sources. The predicted Co-60 point sources match

approximately in total strength and location with the stronger sources in the true line source. From 8–24 detectors, 2–3 of the point sources in the predicted Co-60 line source were resolved. However, DIMP never mapped all five source points of the true Co-60 line source, and typically smeared the locations of the stronger points on the line between the correct cell and a neighbor. This is reasonable because two of the sources are less than 10% of the strongest Co-60 point source. Overall, DIMP performed well once the discrepant detection point was removed from the synthetic-measurement set. Such model discrepancies between DENOVO predicted responses and MCNP synthetic responses are correlated to current limitations in DIMP. The DIMP DRF did not perform well if the detector cell was in-plane with the source cell (including the neighboring cells). In this type of situation, DIMP has a tendency to create false positive or false negative responses for the appropriate directional responses. Adjustments to the current directional DRF are being investigated to relax this limitation.

### 3.3. Experimental results

Four measurement experimental campaigns were conducted at the International Safeguards laboratory at Oak Ridge National

Laboratories (ORNL) using a calibration button point source, an HEU disk calibration source, a set of HEU line sources tied together within a small round duct structure, and a case with multiple HEU sources and fixtures. Each measurement campaign was designed to test and validate source prediction results calculated by the DIMP code system in a specific configuration relevant to the validation of the fundamental methodology for the holdup application. Each campaign's measured results except for the first one will be compared to the current holdup model used in practice at ORNL, HMS-4 (holdup measurement system). This section will discuss the experimental setup including source location, structure, dimensions and composition, and detector location choice rationale.

### 3.3.1. Experimental setup

The activities and active source dimensions of the calibration source are available upon request from the International Safeguards group at Oak Ridge National Laboratories. Note that only the active volume of these sources was simulated in DIMP and not their containers, since attenuation was deemed to be negligible with one exception, the HEU disk. This was encased in a thin layer of stainless steel casing instead of the typical plastic and cardboard casings.

The HEU source record maintained at ORNL reports each source's mass. The uncertainties in the activity were calculated from the mass measurement uncertainty to be about 0.1 %. The emission energies and relative intensities of the gamma-rays of interest for each source used are listed in Table 1.

### 3.3.2. Unshielded Cs-137 button

The first measurement involved only one Cs-137 point source (calibration button source) held above the origin in the selected coordinate system for the computational models by a clamp on a ring stand. This simple experiment was performed to confirm previous results presented by Hykes and Azmy [3]. It was surmised that some of the inconsistency in the previous results could be attributed to weakness of the employed sources. Although the Cs-137 button source is only slightly stronger than the source used by Hykes, it made a good initial source configuration for the calibration of DIMP to the ORNL field detector. In order to minimize the influence of gamma ray scattering by various objects in the lab, a 5-m × 5-m floor space was marked with tape and cleared of all objects deemed nonessential for the experimental measurement. For the vast majority of the measurement time, this remained true. Occasionally, a chair or stool was moved within the measurement boundaries to hold the multichannel analyzer (MCA), or a staff

**Table 1**
Gamma ray energies and relative intensities, with their uncertainties listed in parentheses, of all sources measured were taken from Brookhaven National Laboratory's Nudat2.6 database [11]. Unlisted uncertainties in the database [11] were assumed to be one in the last digit. *Note: gamma-rays from the same source that were within 1 keV of each other were assigned their average energy and their intensities summed together.

| Source | Peak Number | Energy (keV) | Relative Intensity ($) |
|---|---|---|---|
| Am-241 | 1 | 59.5409(1) | 35.9(4) |
| U-235 | 1 | 105.0(1) | 2.00(3)* |
| U-235 | 2 | 109.0(1) | 2.16(13)* |
| U-235 | 3 | 143.76(2) | 10.96(14) |
| U-235 | 4 | 163.356(3) | 5.08(6) |
| U-235 | 5 | 185.715(5) | 57.0(6) |
| U-235 | 6 | 202.12(1) | 1.080(23) |
| U-235 | 7 | 205.316(10) | 5.02(6) |
| Ba-133 | 1 | 80.9979(11) | 35.6(3)* |
| Ba-133 | 2 | 356.0129(7) | 62.05(1) |
| Cs-137 | 1 | 661.657(3) | 85.10(20) |
| Co-60 | 1 | 1,173.228(3) | 99.85(3) |
| Co-60 | 2 | 1,332.492(4) | 99.9825(6) |

**Table 2**
Coordinate locations of the center point of the detector face for each measurement of the Cs-137 point source. The origin is located on the floor at the very center of the cleared square. The uncertainty in each measurement coordinate is 1 mm.

| Measurement # | Location (cm) | Total Distance | Detector Orientation |
|---|---|---|---|
| Source | (0,0,87) | 0 | |
| 1 | (51,140,87) | 149.0 | −y |
| 2 | (120,32,77) | 124.6 | −x |
| 3 | (100,−20,96) | 102.4 | −x |
| 4 | (10,−74,81) | 74.9 | +y |
| 5 | (−5,−60,93) | 60.5 | +y |
| 6 | (−50,0,97) | 51.0 | +x |
| 7 | (−40,16,84) | 43.2 | +x |
| 8 | (−7,20,89) | 21.3 | −y |
| 9 | (3,10,87) | 10.4 | −y |
| 10 | (2,0.3,87) | 2.02 | −x |

member walked through the marked zone inadvertently. However, the effect of these infractions on the precision of the measured response is considered negligible as no foreign object (including the chair carrying the MCA) remained in the field of view of the detector for any significant length of the measurement time.

The equipment deployed in conducting the experiment included two ring stands, a 2-inch × 1-inch NaI detector, and a Cs-137 calibration source. The stands each had a pole approximately 1.5 m tall with a diameter of 2 cm, and a rectangular base (0.27 m × 0.16 m). The list of coordinate locations of the center-point of the face of the detector for each detector measurement, and the source location are shown in Table 2.

The next validation experiment involved measuring a larger HEU source that could either be treated as an area source (multiple cells in a block) or a single cell source depending on the mesh resolution. This source again was held above the origin of the measurement area by a clamp on a ring stand. This allowed for measuring a more relevant radiation source to holdup and calibrating DIMP to HEU sources without significantly increasing the complexity of the source geometry. The detector measurement coordinates and the coordinates of the center of the HEU disk source are shown in Table 3. A photograph of the experimental setup is presented in Fig. 7.

The next set of experiments involved the arrangement of various HEU sources within three steel fixtures on carts to simulate realistic holdup in a facility environment. The three fixtures were: a small round duct, an L-duct, and a pipe array. Each cart is a metal dolly with wheels and steel strut supports to hold the fixture in place. The pipe array is not included because it was never filled with a source. The HEU measurements will be included in future publications once the validation analysis is completed.

**Table 3**
Coordinate locations of the detector face for each measurement of the HEU Disk source. The uncertainty in each measurement coordinate is 1 mm.

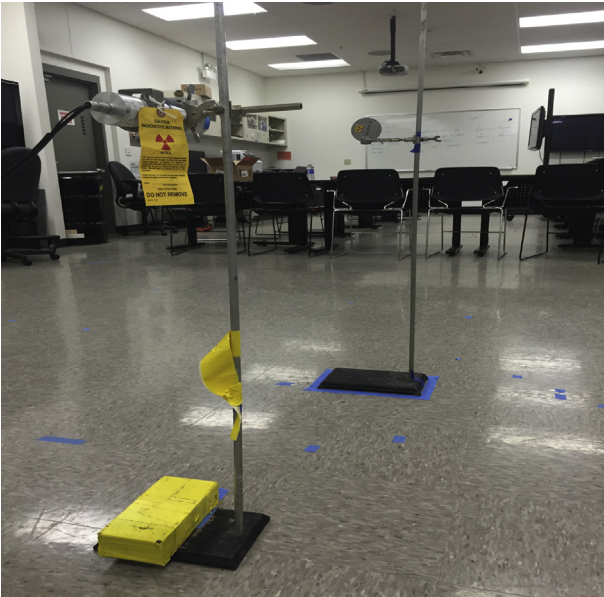| Measurement # | Location (cm) | Total Distance | Detector Orientation |
|---|---|---|---|
| Source | (0,0,91) | 0 | |
| 1 | (100,−20,100) | 102.4 | −x |
| 2 | (16,−40,88) | 43.2 | +y |
| 3 | (5,−50,95) | 50.4 | +y |
| 4 | (−60,−5,97) | 60.5 | +x |
| 5 | (−74,10,85) | 74.9 | +x |
| 6 | (−7,20,93) | 21.3 | −y |
| 7 | (3,10,91) | 10.4 | −y |
| 8 | (2,0.3,91) | 2.02 | −x |
| 9 | (40,0,91) | 40.0 | −x |
| 10 | (6,−1,91) | 6.08 | −x |

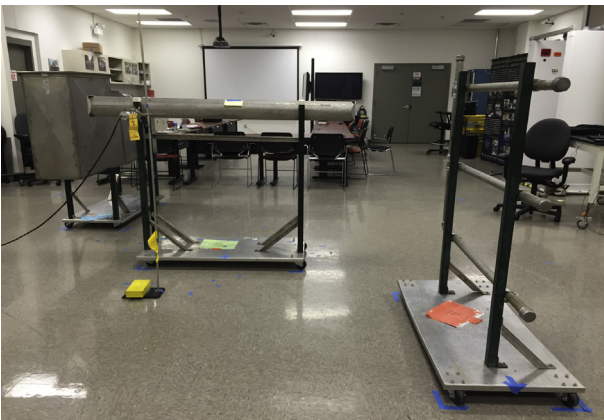**Fig. 7.** Photograph of the HEU Disk source measurement experimental setup.



**Fig. 8.** Photograph of the general holdup-like source measurement experimental setup.

A photograph of the general experimental setup is included for perspective in Fig. 8.

### 3.3.3. Simulation experimental geometry

The base simulation geometry for all experiments included a main void region on top of a floor region which was composed of a standard tile and concrete mixture across a 5-m × 5-m square area. The cells were contained between −2.5 m on the west boundary to +2.5 m on the east boundary. The same is true for −2.5 m from the south boundary and ending at +2.5 m at the north boundary. The origin was in the center, just above the upper floor surface boundary. The z-axis is defined from −10 cm (the underside of the floor) to 3 m above the floor. For DENOVO, each cell (e.g., floor, steel fixtures, ring stand, etc.) is simulated with parallelepipeds to approximate all of the necessary surfaces in Cartesian geometry, as DENOVO does not permit curved surfaces. However, curved surfaces were employed in the synthetic response simulations to model the detector and the geometric arrangement executed by MCNP.

Though the physical geometry of the detector is simulated in MCNP, it is not simulated in DENOVO. Instead, the response values were taken at the center face of the detector after multiplying the adjoint source by a point DRF factor to approximate the effects of the shielding and collimator. The current point DRF formulation used by DIMP is described by Hykes [8].

### 3.3.4. Experimental measurement equipment

The field equipment used to take measurements for all experimental campaigns included a detector with a pre-amplifier and a multichannel analyzer with full pulse processing integration. Both pieces of equipment were essential for HMS-4 and DIMP holdup measurements.

The detector was a 1-inch-diameter by 2-inch-height right cylinder EFC Model 1X2P collimated NaI scintillation detector. This is a standard field detector for HMS-4 measurements [12]. The detector is well shielded with lead, except on the front face where the collimator aperture allows radiation into the detector from a limited extent of directions, i.e., fixed solid angle. Hence, the detector has approximately a 23 degree in-axial-plane angle of vision from the axis normal to its circular front face.

The MCA was a GBS Elektronik GmbH MCA-166 Rossendorf model [13] that has a self-contained set of pulse processing equipment. The MCA receives a pre-amplified signal directly from the detector through a coaxial cable, which it amplifies and counts across a spectrum of energies. The number of counts is divided into channels (proportional to energy) and sent directly to the computer for recording and post-processing.

### 3.4. Cs-137 point source

DIMP performed fairly well for the first validation exercise using ORNL experimental measurements involving the Cs-137 point source after some adjustments. Under the standard initial guess ($\alpha = 10^{-4}$, the baseline static weak source cell probability), DIMP failed to predict any source cells with magnitude larger than 1% of the true source strength. However, using the true source configuration as the initial guess yielded a very good result alluding to DIMP becoming trapped in a local minimum during the first source search. The usual initial guess was chosen with a flat low source probability in every mesh cell allowing feedback with the measured responses to increase the source probability in the appropriate cells. Furthermore, a correction factor had to be applied to the measured responses to account for the effects observed as a result of the special collimator geometry for ORNL's 1-inch × 2-inch NaI field holdup detector, that were not featured in the previous detector design used in Ref [2] and utilized in the synthetic data presented in previous sections of this paper. Additionally, two measurement points had higher than expected flux values, so further investigation is currently underway to determine if they are statistical outliers or whether further adjustments to the detector model need be made.

### 3.4.1. Development of the collimation correction factor

The detector used by Hykes and Azmy [3] was a 2-inch × 2-inch NaI detector, collimated by the placement of lead bricks above and to the sides of the detector to produce a forward-facing hemisphere field of view (FOV). The 1-inch × 2-inch NaI field holdup detector provided by ORNL to conduct the measurement campaigns has a much more sophisticated collimator that narrows the FOV to roughly 23 degrees and partially obscures the crystal face. The front of the lead collimator touches the crystal face and covers about 12% of the face, reducing the detector's solid angle FOV. Since the previous configuration [3] did not suffer such a reduction in solid angle, DIMP required a collimation correction factor to adjust the detector efficiency for the effect of this collimation on the directional responses. The source-location dependent reduction in solid angle is illustrated by Fig. 9
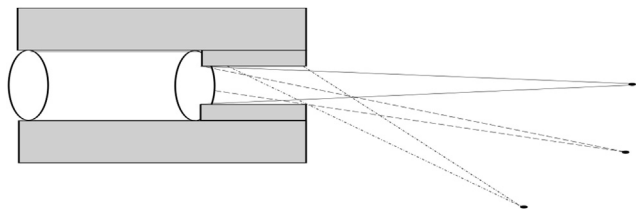
**Fig. 9.** Sketch of the detector collimator shadowing effect on the detector crystal (reducing the effective solid angle).

A fairly simple way to compute such a factor, is to simulate the detector with and without the collimator geometry (just the detector crystal) in MCNP and compare the results to the analytical solid angle calculations. Using the ratio of the two scalar fluxes (with and without the collimator) averaged over the crystal volume as the collimation correction factor, the measured responses can be corrected by this factor to better match the responses predicted by the true source distribution folded with DENOVO adjoint fluxes. Thus, the collimation correction factor ($S_{col}(\mathbf{r},E)$) can be calculated as follows

$$S_{col}(\mathbf{r}, E) = \frac{\phi_{col}^{syn}(\mathbf{r}, E)}{\phi_{unc}^{syn}(\mathbf{r}, E)} \qquad (25)$$

where $\phi_{col}^{syn}(\mathbf{r}, E)$ and $\phi_{unc}^{syn}(\mathbf{r}, E)$ are the collimated and uncollimated synthetic responses calculated from the true source configuration in MCNP. Dividing the measured responses by $S_{col}(\mathbf{r},E)$ will produce an approximate value of the response that would have been measured with a $2\pi$ FOV detector that is assumed in the current version of DIMP. A more rigorous way to account for the collimator's effect is to determine a directionally dependent DRF.

The correction factor was used to adjust each of the measured responses from the Cs-137 point source campaign before initializing DIMP's source search algorithm. The experiment involved ten detection points measured within the experimental area in a spiral pattern around the 4 $\mu$Ci point source held by a clamp on the ring stand (similar to the HEU setup in Fig. 7). The distance between the source and detection points ranged from 0.02–1.25 m as discussed in the previous section, and the coordinates of the true Cs-137 point source are (0,0,87) cm. Note, the spiral pattern was chosen to ensure that the detector received sufficient source signal in order to prevent excessive count times, and current software and detector response function limitations prevented the measurement of the source from angles offset from the Cartesian coordinate axes. Within these limitations, the spiral pattern was a prudent way to vary source-to-detector distance without duplicating detector response information.

Consider the DIMP predicted source map shown in Fig. 10 of Appendix I. As in this source-strength map, DIMP performed well predicting the source in the correct cell centered at (0,0,90) with 97% of the true source activity with fairly low uncertainty. Only 97% of the true source strength was obtained because the FOV-corrected measured responses still had a margin of error when compared with those calculated by DENOVO. This is a promising result for the first of the four experimental measurements, but there are two issues. The first is that, as in Hykes and Azmy's study [3], the source search had to be narrowed to a lower number of mesh cells in order to find a good source configuration. Specifically, instead of allowing the point source to occupy any number of cells within the full volume of air in the problem configuration

(100 $\times$ 100 $\times$ 61 cells), we limited the region where the source can be located to 40 $\times$ 40 $\times$ 30. Otherwise, the gradient source search algorithm often became stuck in local minima and predicted weak distributed sources with larger values of the reduced chi-squared. The second is that two detection point fluxes did not match up with MCNP synthetic fluxes, so for the time being they were adjusted to the synthetic values artificially. Further investigation will determine a physical explanation for those discrepant values if possible. They may be removed as outliers, since both points were measured fairly close to the source.

## 4. Conclusions

DIMP is a reliable inverse radiation transport solver that has proven to be stable for point and line radiation source configurations. Although DIMP does not resolve the entire line source with full accuracy, it still approximates the strong point sources in the line well. DIMP maps the source within a few cells of its true location and generally predicts the correct source strength when using more than five detection points.

DIMP performed fairly well for the first validation exercise concerning the Cs-137 point source suspended by a clamp stand once a detector collimation factor was applied to the measured responses and the spatial domain for the source search was reduced by 90% (a full order of magnitude). Without the domain reduction, DIMP's optimizer often failed to predict the correct source because it became stuck in local minima that were less optimal than the true source specification as quantified by the corresponding reduced chi-squared values. With the success of the reduced-volume search, it can be concluded that future DIMP optimization searches should be attempted with either an alternate optimizer that does not easily become trapped in local minima, or an adaptive mesh algorithm be applied to reduce the search spatial domain to only logically acceptable source cells (in equipment, not floors, walls, random air cells, etc.).

DIMP is expected to perform well for the remaining validation exercises. DIMP will also be verified against SNM masses predicted by ORNL's HMS-4 system. The validation will consist of three additional measurements already conducted over experimental campaigns involving two single source cases and one multi-source case in various geometries. Two of the campaigns were meant to simulate holdup-like sources in a realistic facility geometry (e.g., sources in pipes and ducts), while the others were used for calibration of the DIMP system.

## Conflicts of interest

None.

## Acknowledgments

## Appendix I



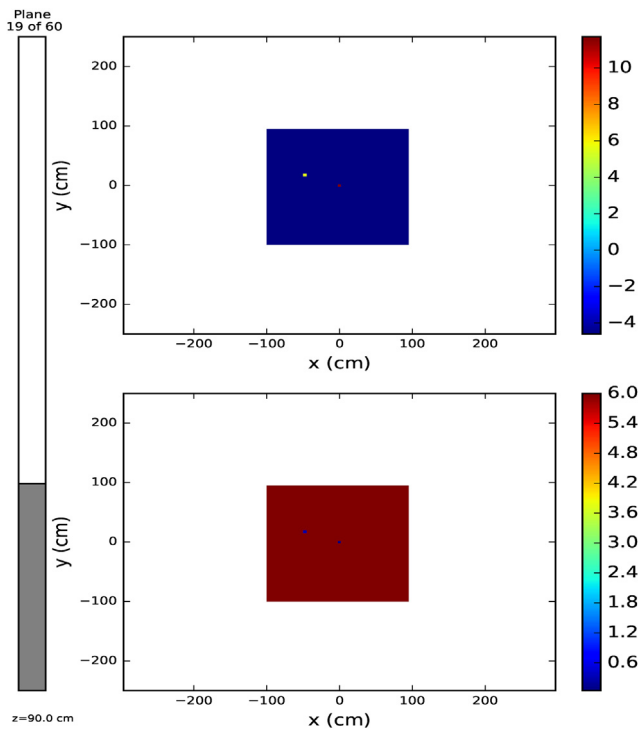**Fig. 10.** DIMP predicted source-strength map (above) for a 5-m × 5-m square space (reduced to a 2-m × 2-m search area) with a Cs-137 point source suspended by clamps on a ring stand, and the corresponding uncertainty (below).

## References

[1] N. Nelson, Y. Azmy, Numerical convergence and validation of the DIMP inverse particle transport model. International Conference on Mathematics & Computational Methods Applied to Nuclear Science & Engineering, Jeju, Korea, April 16–20, 2017.

[2] T.D. Reilly, Nondestructive assay of holdup, in: Passive Nondestructive Assay of Nuclear Materials 2007 Addendum, Los Alamos National Laboratory, Washington DC, 2007.

[3] J.M. Hykes, Y. Azmy, Radiation source mapping with Bayesian inverse methods, Nucl. Sci. Eng. 179 (2015) 1–17.

[4] A. Tarantola, Inverse Problem Theory and Methods for Model Parameter Estimation, Society for Industrial and Applied Mathematics, Philadelphia, 2005.

[5] D.G. Cacuci, M. Jonescu-Bujor, Sensitivity and uncertainty analysis, data assimilation, and predictive best-estimate model calibration, in: Handbook of Nuclear Engineering, Springer, New York, 2010.

[6] E.E. Lewis, W.F. Miller Jr., Computational Methods of Neutron Transport, American Nuclear Society, La Grange Park, IL, 1993.

[7] Scale: A Comprehensive Modeling and Simulation Suite for Nuclear Safety Analysis and Design, ORNL/TM-2005/39, June 2011. Available from Radiation Safety Information Computational Center at Oak Ridge National Laboratory as CCC-785, Version 6.1.

[8] J. Hykes, Radiation Source Mapping with Bayesian Inverse Methods, PhD Thesis, North Carolina State University, 2012.

[9] R.P. Gardner, A. Sood, A Monte Carlo simulation approach for generating NaI detector response functions (DRFs) that accounts for nonlinearity and variable flat continua, Nucl. Instrum. Meth. Phys. Res. B 213 (2004) 87–99.

[10] N. Nelson, Validation and Uncertainty Quantification of a 1 × 2" NaI Collimated Detector Using Detector Response Functions Created by g03, MS Thesis, North Carolina State University, 2014.

[11] National Nuclear Data Center [Internet], Nudat2.6: Decay Radiation Search, Brookhaven National Laboratory, 2013 [Accessed 2015 Jun 14]. Available from: http://www.nndc.bnl.gov/nudat2/indx_dec.jsp.

[12] S.E. Smith, K.A. Thompson, J. Malcom, P.A. Russo [Internet], Holdup Measurement System 4 (HMS4)-Automation & Improved Accuracy BWXT Y-12 Report Y/DK-2190, ORTEC, 2004 [Accessed 2016 Aug 16]. Available from: http://www.ortec-online.com.

[13] GBS Elektronik GmbH, MCA 166-USB: Multi Channel Analyzer with USB Interface, GroBerkmannsdorf, Germany, 2008.